PHYSICAL REVIEW RESEARCH **3**, 043007 (2021)

Editors' Suggestion

Quantum sensing of photonic spin density using a single spin qubit

Farid Kalhor,[1,*] Li-Ping Yang,[1,2,*] Leif Bauer,[1] and Zubin Jacob[1,†]
[1]*School of Electrical and Computer Engineering, Purdue University, West Lafayette, Indiana 47906, USA*
[2]*Center for Quantum Sciences and School of Physics, Northeast Normal University, Changchun 130024, China*

(Received 30 June 2021; revised 12 August 2021; accepted 6 September 2021; published 1 October 2021)

Nitrogen-vacancy (NV) centers in diamond have emerged as promising room-temperature quantum sensors for probing condensed matter phenomena ranging from spin liquids, two-dimensional (2D) magnetic materials, and magnons to hydrodynamic flow of current. Here we propose and demonstrate that the nitrogen-vacancy center in diamond can be used as a quantum sensor for detecting the photonic spin density, the spatial distribution of light's spin angular momentum. We exploit a single spin qubit on an atomic force microscope tip to probe the spinning field of an incident Gaussian light beam. The spinning field of light induces an effective static magnetic field in the single spin qubit probe. We perform room-temperature sensing using Bloch sphere operations driven by a microwave field (XY8 protocol). This nanoscale quantum magnetometer can measure the local polarization of light in ultra-sub-wavelength volumes. We also put forth a rigorous theory of the experimentally measured phase change using the NV center Hamiltonian and perturbation theory involving only virtual photon transitions. The direct detection of the photonic spin density at the nanoscale using NV centers in diamond opens interesting quantum metrological avenues for studying exotic phases of photons, nanoscale properties of structured light as well as future on-chip applications in spin quantum electrodynamics.

DOI: 10.1103/PhysRevResearch.3.043007

I. INTRODUCTION

Nitrogen-vacancy (NV) centers in diamond have been used to probe electron spin excitations in matter such as magnons [1], magnetic thin films [2], and magnetic skyrmions [3]. Even in nonmagnetic materials such as plasmonic silver; low-frequency evanescent wave Johnson noise and ballistic transport of electrons can be probed by NV centers [4]. NV centers in diamond can also work as navigation guidance systems by vector sensing of earth's magnetic field [5]. This emerging frontier of research shows how coherence in spin qubits allows for ultrasensitive read-out of magnetic fields and magnetic noise in quantum materials and beyond. It is therefore intriguing to explore how the synthetic magnetic fields generated by light can be probed using the same quantum metrological principles. Here, we put forth the concept of quantum metrology of a property of dynamical light fields at room temperature.

We propose and demonstrate that NV centers in diamond can sense the local polarization of spinning light fields within ultrasmall mode volumes. Our sensor is a single spin qubit interacting with the effective static magnetic field generated by a circularly polarized light field. We measure the induced phase of the spin qubit through optical read out to directly detect the photonic spin density (PSD) of a laser beam red-detuned to the optical transition of the NV center. We demonstrate coherent interaction at room temperature paving the way to probe exotic spin states of photons. We also put forth a rigorous theory of interaction between photon spin density and the spin qubit using the full NV center Hamiltonian. Finally, we shed light on how on-chip nanophotonic structures possess effective static magnetic fields arising from the intrinsic spin of evanescent waves. This effect can be exploited in future spin quantum electrodynamics devices for on-chip targeted addressing of spin qubits.

The spinning field of light has long been associated with the concept of global polarization [6,7]. Here the spin angular momentum (SAM) of light is a vector with its direction pinned parallel to the momentum of a far field propagating wave. In stark contrast, the PSD has only recently emerged to the forefront of nanophotonics [8–12]. PSD in confined or structured light beyond the traditional paraxial regime can exhibit exotic spatial variation of local polarization known as spin texture [13]. In recent years, exploring the near-field properties of this spin texture has led to the discovery of exotic phenomena such as photonic skyrmions and topological electromagnetic phases of matter [14–16].

Interesting phenomena originating from near-field photon spin density include directional spontaneous emission, one-way scattering of surface plasmon polaritons, transverse spin in free space light beams, and anomalous optical forces [17–21]. Here the nature of PSD is inferred indirectly through directional phenomena, i.e., spin-momentum locking or spin to orbital angular momentum conversion [22–24]. We note that the orbital angular momentum (OAM) of light is an ex-

---

[*] These authors contributed equally to this work.

[†] zjacob@purdue.edu

trinsic degree of freedom that can be directly detected due to its wavelength scale helical phase signatures [25]. However, direct measurement of PSD remains a challenge since the fundamental property of photon spin density exists in subwavelength volumes of the light field. Therefore, there is an urgent need to develop a nanoscale photon spin probe similar to near-field scanning optical microscopy [12,20] routinely used to detect dipolar electric fields or magnetic force microscopy which can map nanoscale texture of electron spins.

II. THEORETICAL MODEL OF SPIN QUBIT INTERACTING WITH PHOTONIC SPIN DENSITY

In order to demonstrate the ultra-sub-wavelength probing of PSD, we study the interaction between the spin of a monochromatic optical beam and an NV center that is placed on an atomic force microscopy (AFM) tip. This is a versatile system for future explorations of spin texture of complex optical beams. We note that the light-matter interaction between the Gaussian beam and the spin qubit only occurs due to virtual photon transitions since our incident beam is far detuned from the energy levels of the NV center. Thus the signature of the PSD is in the phase of the single spin qubit. We therefore need quantum metrological tools to quantify this unique coherent light-qubit interaction at room temperature.

In classical electrodynamics (CED), the total angular momentum of charged particles and electromagnetic fields are given by $\vec{J}_{\text{CED}} = \sum_\alpha \vec{x}_\alpha \times \vec{p}_\alpha + \epsilon \int d^3x \vec{\mathcal{E}}_\perp \times \vec{A}_\perp + \epsilon \int d^3x \mathcal{E}_\perp^j (\boldsymbol{x} \times \nabla) A_\perp^j$ (see chap. I in Ref. [26]), where $\vec{\mathcal{E}}(\vec{r}, t)$ is the electric field, $\vec{A}(\vec{r}, t)$ is the vector potential, the subindex $_\perp$ denotes the transverse part of the vector field, and ϵ is the permittivity. These three terms denote the OAM of the charges, SAM of light, and OAM of light, respectively. In this equation, the integral kernels give the photonic spin and OAM densities. While the term SAM is also used to describe the kernel of the SAM term in the literature, we use the term PSD for the kernel to distinguish it from the SAM. Our goal is to emphasize on the local and nanoscale characteristics of it. In this work, we demonstrate a technique that can be used to measure the PSD $\vec{S}^{\text{obs}} = \epsilon \vec{\mathcal{E}}_\perp(\vec{r}, t) \times \vec{A}_\perp(\vec{r}, t)$ [27] with nanoscale resolution using a single NV center in diamond.

For a monochromatic beam with frequency ω_0, the PSD can be written as $\vec{S}^{\text{obs}} = (1/4\omega_0)\text{Im}[\epsilon \vec{E}^* \times \vec{E} + \mu \vec{H}^* \times \vec{H}] = \vec{S}_E^{\text{obs}} + \vec{S}_M^{\text{obs}}$ where $\vec{E}^*(\vec{H}^*)$ denotes the complex conjugate of the complex electric (magnetic) field [28,29], i.e., $\vec{\mathcal{E}}_\perp = (\vec{E} + \vec{E}^*)/2$. The PSD is time independent and is related to the handedness of the polarization of the beam. According to the selection rules of electric-dipole transitions, circularly polarized light will change the electronic orbital angular momentum by $\pm\hbar$ while keeping the electron-spin state unchanged. However, due to spin-orbit coupling, the transition frequencies in the NV center become dependent on the electron spin states as shown in Fig. 1(b). Under a detuned incident light beam, virtual electric-dipole transitions will induce ac Stark shifts in the ground electronic state [30–33]. As illustrated in Figs. 1(c) and 1(d), the amplitude of these shifts (δ_0 and $\delta_{\pm 1}$) depend on both the electronic spin state of the NV center and the photonic spin density of the excitation. We show that this effect manifests itself as a PSD dependent effective static magnetic field. We exploit the single NV center as a nanoscale quantum magnetometer [34] to measure this effective static magnetic field created by the target spinning light.

We consider the detailed energy level structure of NV centers in the basis of RCP and LCP transitions to express the net energy shift as a function of PSD. The effective excited-state Hamiltonian of the NV center is given by [35,36],

$$\begin{aligned} H_{\text{ES}} = {} & (\gamma_{\text{NV}} B + \Delta_{\text{es}} + \lambda_z)|A_\uparrow\rangle\langle A_\uparrow| \\ & + (-\gamma_{\text{NV}} B + \Delta_{\text{es}} + \lambda_z)|A_\downarrow\rangle\langle A_\downarrow| - 2\Delta_{\text{es}}|E_R\rangle\langle E_R| \\ & - 2\Delta_{\text{es}}|E_L\rangle\langle E_L| + (\gamma_{\text{NV}} B + \Delta_{\text{es}} - \lambda_z)|E_\uparrow\rangle\langle E_\uparrow| \\ & + (-\gamma_{\text{NV}} B + \Delta_{\text{es}} - \lambda_z)|E_\downarrow\rangle\langle E_\downarrow|, \end{aligned} \tag{1}$$

where $\gamma_{\text{NV}} = 2\pi \times 28$ MHz/mT, B is the external static magnetic field, $\lambda_z \approx 2\pi \times 5.5$ GHz is the spin-orbit coupling, and $\Delta_{\text{es}} \approx 2\pi \times 1.42/3$ GHz is the spin-spin-induced zero-field splitting. $|A_\uparrow\rangle$, $|A_\downarrow\rangle$, $|E_R\rangle$, $|E_L\rangle$, $|E_\uparrow\rangle$, and $|E_\downarrow\rangle$ are spin and orbital angular momentum resolved excited states shown in Fig. 1(b). Using second-order perturbation theory, ac Stark shift for the ground-state energy levels is [30,37],

$$\delta_i = \frac{1}{4\hbar^2} \sum_f \frac{|\langle f|\vec{d}|i\rangle \cdot \vec{E}(\vec{r}, t)|^2}{\Delta_{\text{if}} + \Gamma_f^2/4\Delta_{\text{if}}}. \tag{2}$$

where $|i\rangle$ and $|f\rangle$ are the initial and final states for all possible transitions, Δ_{ij} is the difference between the center frequency of the off-resonant excitation (ω_0) and the resonance frequency of the transition (ω_{ij}), and Γ_f is the spontaneous decay rate of the final state. Using the Hamiltonian in Eq. (1) and the transition rules for circularly polarized incident light, we arrive at the result of the effective static magnetic field generated by spin density of light (see Appendix A):

$$B_{\text{eff}} \equiv \frac{\delta_{+1} - \delta_{-1}}{2\gamma_{\text{NV}}} \propto \vec{S}_E^{\text{obs}} \cdot \hat{n}, \tag{3}$$

where $\hat{n}$ is the direction of the NV center. From Eq. (3), we see that the strength of the effective static magnetic field is proportional to the projection of the electric PSD ($\vec{S}_E^{\text{obs}}$) on the NV center axis ($\hat{n}$). In the expression above, we have used the spin states $|\pm 1\rangle$ to form the probe qubit as it leads to effective static magnetic fields directly proportional to the PSD. One can also use $|0\rangle \leftrightarrow |\pm 1\rangle$ transitions as the probe qubit. We show a comparison between the choice of probe qubits in Fig. 2(c). The magnetic portion of the PSD ($\vec{S}_M^{\text{obs}}$) does not interact with the NV center since the optical transitions are derived by electric dipole interactions.

The PSD of the target beam is determined by its power and degree of circular polarization. In our experiment, the wavelength of the target beam is $\lambda_0 = 800$ nm, which is far off-resonant to the optical transition of the NV center at $\lambda = 637$ nm [Fig. 1(b)]. We control the PSD by tuning the power of the beam and the angle θ between the linear polarizer and the quarter-wave plate (QWP) [see Fig. 2(a)]. The degree of circular polarization (i.e., the photonic spin density) is $\vec{S}_E^{\text{obs}} \propto \sin(2\theta)\hat{z}$, where $\hat{z}$ is the direction of propagation of the beam. Equation (3) shows that an NV center can only sense the projection of a magnetic field on its defect axis. Therefore, the measured effective static magnetic field also

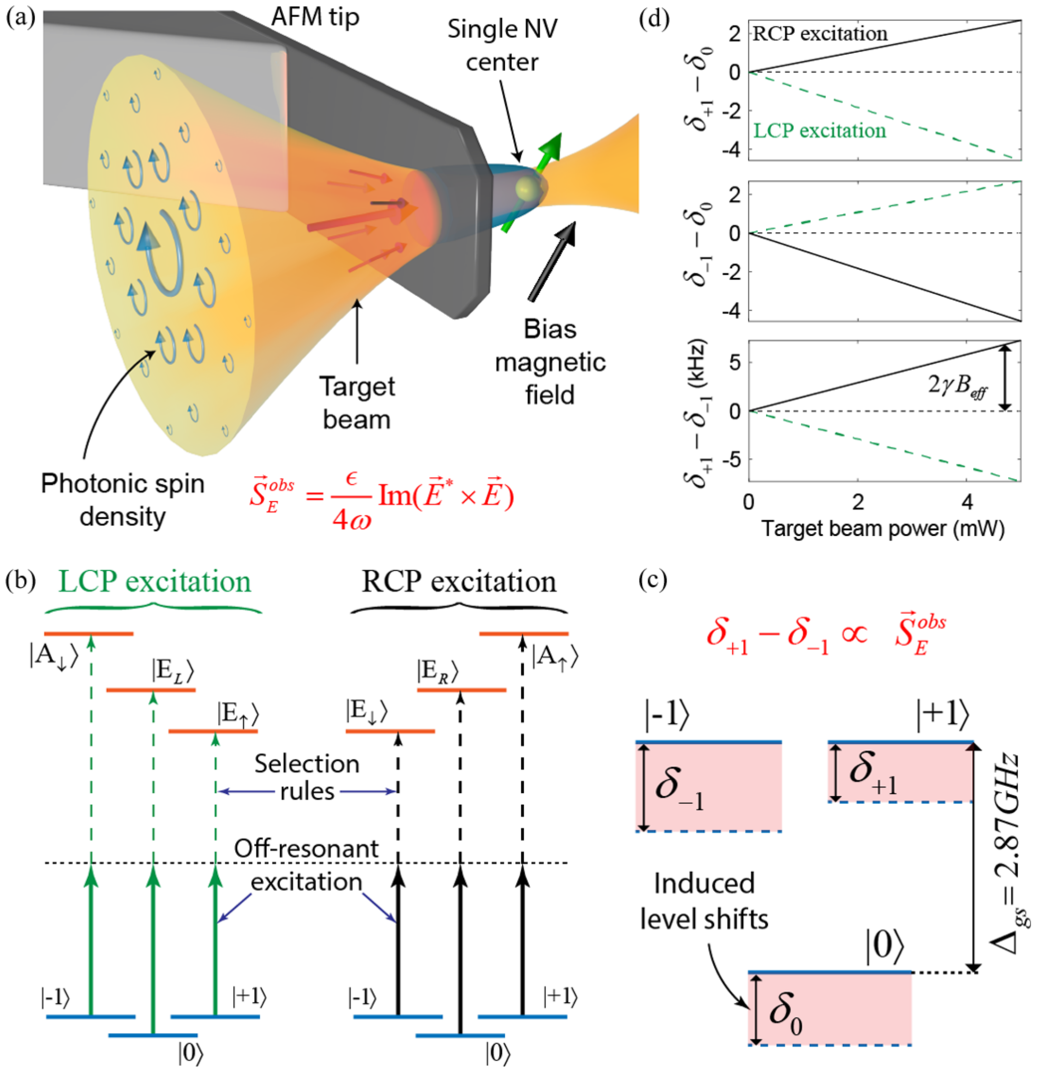

FIG. 1. Probing PSD with a single NV center. (a) A target beam, red-detuned to the NV center transition, is incident on a single NV center on an AFM tip. We measure the relative energy level shifts in the ground state and show its proportionality to the PSD. The single NV center serves as a room-temperature nanoscale probe for PSD. (b) Ground- and excited-state energy levels of an NV center showing the selection rules for RCP and LCP excitation. (c) Level shifts induced in the ground state due to the virtual transitions under the off-resonant target beam. (d) Power and polarization (spin) dependence of the relative energy shifts in the ground state, resembling Zeeman splitting. An effective static magnetic field is defined as $B_{\mathrm{eff}} = (\delta_{+1} - \delta_{-1})/2\gamma$.

depends on the alignment angle ϕ between the NV center axis and the PSD vector. We show the theoretical simulation of the effective static magnetic field B_{eff} sensed by an NV center, as a function of θ and ϕ in Fig. 2(b). We should note that in the experimental results, the alignment angle is fixed at $\phi = 54.7^\circ$ due to the growth angle of the diamond crystal. For this specific angle, we show the effective magnetic field experienced by the probe qubit in Fig. 2(c). This variation of the effective static magnetic field with degree of circular polarization is the unique signature of PSD. We note that the target laser is red-detuned to the optical transition of the NV center and is not absorbed by the NV center. Therefore, the resulting effective static magnetic field is not due to the absorption or emission related spectral features of the NV center. It is related to the induced phase in the spin qubit measured by optical read out.

III. EXPERIMENTAL DEMONSTRATION USING A SINGLE NV CENTER

We overcome the challenge of room-temperature observation of PSD to pave the way for future on-chip applications. We exploit a large detuning of the target PSD beam to the optical transition of the NV center to avoid absorption of photons by the NV center which would result in a loss of coherence. This detuning results in an amplitude of a few tens of nanotesla for the generated effective static magnetic field. In order to probe this effective magnetic field at the location of the single NV center, we use ac magnetometry techniques at room temperature. In ac magnetometry, high sensitivity is achieved due to a long coherence time from spectral filtering of magnetic fluctuations (e.g., nuclear noise) coupled to the NV center [38,39]. Figure 3 shows the dynamics of the mea-

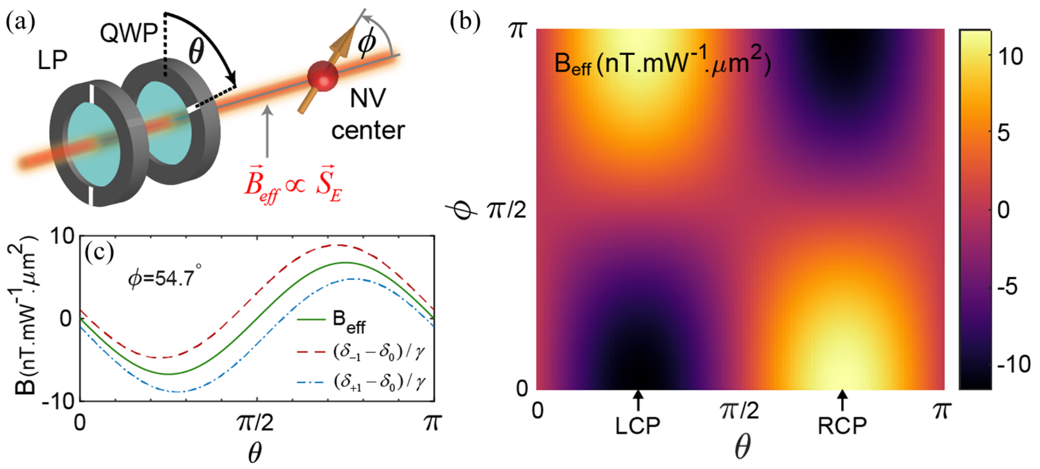

FIG. 2. Effective static magnetic field induced by PSD. (a) A linear polarizer and a quarter wave plate control the PSD. (b) The effective magnetic field calculated for different QWP angles (θ) and alignment angles (ϕ). (c) The effective magnetic field calculated for an NV center in a (100) cut diamond, $\phi = 54.7^\circ$.

surements. A 532-nm laser is used to initialize and readout the state of the qubit. After initialization, a series of microwave pulses are sent in XY8 configuration to achieve dynamical decoupling of the qubit from background noise [40]. The intensity of the target beam is modulated to match the frequency of the XY8 pulse for ac magnetometry. Furthermore, we perform two measurements for which the phase induced by the PSD has opposite signs [Fig. 3(e) and 3(f)]. This is achieved by taking advantage of the sign of an ac field as show in Fig. 3(a). We suppress the effect of any systematic noise by subtracting the outcome of these two measurements. The parameters used in the measurements are shown in Table I.

The first striking evidence of photonic spin density measurement is shown in Fig. 4(c). We observe that the effective static magnetic field generated by PSD directly follows the ellipticity of the polarization of the target beam. For a Gaussian beam, the PSD is proportional to the degree of ellipticity of the polarization. In our experiment, we control the ellipticity

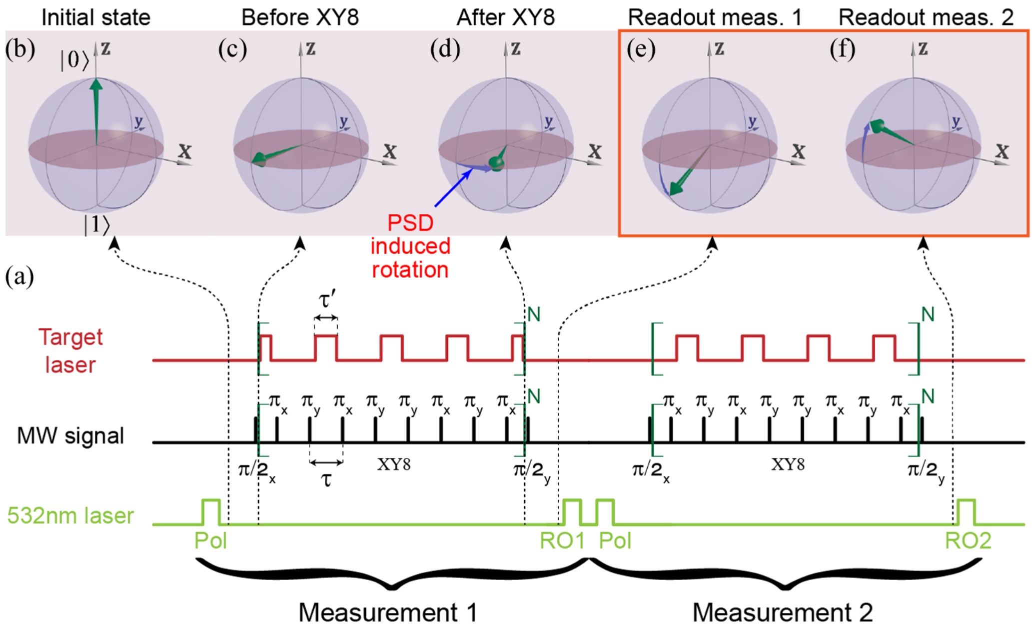

FIG. 3. Isolating the signature of photonic spin density using dynamical decoupling and ac magnetometry with a single spin qubit. (a) Pulse sequence used for measuring the PSD. In each measurement a pair of 532-nm laser pulses initialize (polarize) and readout the state of the NV center. During each measurement an XY8 MW pulse performs dynamical decoupling on the spin of the NV center. The target beam, generating the PSD, is turned on and off during the XY8 sequence to generate a net effect on the final state of the NV center. We perform two measurements in which the target beam induces rotations in opposite directions on the spin vector in the Bloch sphere. By subtracting the outcome of these two measurement we eliminate any systematic noise in the measurement. [(b)–(f)] Bloch sphere representation of the state of the qubit after polarization, before the XY8 pulse, after the XY8 pulse, and before readout. Panels (e) and (f) show an schematic comparison between the PSD-induced rotations in measurement 1 and measurement 2. The PSD is generated by the target beam. RO, readout; Pol, polarizing.

TABLE I. Dynamical decoupling measurement parameters used for the results shown in Fig. 4.

Number of XY8 repetitions	4
Free precession time (τ)	1.2 μs
Total sequence time	~40 μs
Target beam pulse length (τ')	1 μs
Total interaction time	15 μs
π-pulse length	~50 ns

of the target beam using a linear polarizer and QWP. Fig. 4(c) shows the observed dependence of the effective static magnetic field on the angle of the QWP (θ). Also plotted are a sinusoidal fit of the data (red dashed curve) and the result of full wave numerical simulations (purple curve). The data shows a small dc offset in the curve which is not present in Eq. (1). This offset is related to an asymmetry in the system's geometry, which would lead to the presence of transverse spin at the location of the NV center. This transverse spin obeys spin-momentum locking rules [8,17] and does not depend on the QWP angle and therefore, gives rise to the offset (see Appendix E).

The second convincing proof of PSD measurement is the linear dependence of the effective static magnetic field on the power of the beam [Eq. (3)] shown in Fig. 4(d). The PSD is linearly proportional to the power of the beam. This is in contrast to real magnetic fields where the amplitude scales with the square root of the power. The dashed red line shows a linear fit to the measured data. It should be noted that for each data point in Figs. 4(c) and 4(d) we measure the energy shifts $\delta_{\pm 1} - \delta_0$ separately and calculate the effective static magnetic field B_{eff} according to Eq. (3). The inset of these figures show the raw data for these measurements.

These two unique features in the measured effective static magnetic field also show that the measured quantity is not affected by temperature oscillations in the diamond caused by the target laser. A change in the temperature of the diamond can also lead to a shift in the energy levels of the NV center [41]. However, this effect is distinguishable from the effective static magnetic field induced by the PSD because the induced temperature oscillation is independent of the polarization of the beam while the PSD-induced effect depend on the degree of ellipticity of the beam as shown in Figs. 4(c). The results in Figs. 4(c) and 4(d) do not show any significant temperature oscillations in the sample.

IV. EFFECTIVE STATIC MAGNETIC FIELD IN OPTICAL WAVEGUIDES

We now discuss how this universal photonic spin density-induced effective static magnetic fields can be used in future generation of on-chip spin QED applications. We note that evanescent waves are a ubiquitous resource available on a scalable nanophotonic platform. These evanescent waves possess an intrinsic universal spin that can exert effective static magnetic fields on spin qubits with a subwavelength resolution. This effective magnetic field is only manifested on

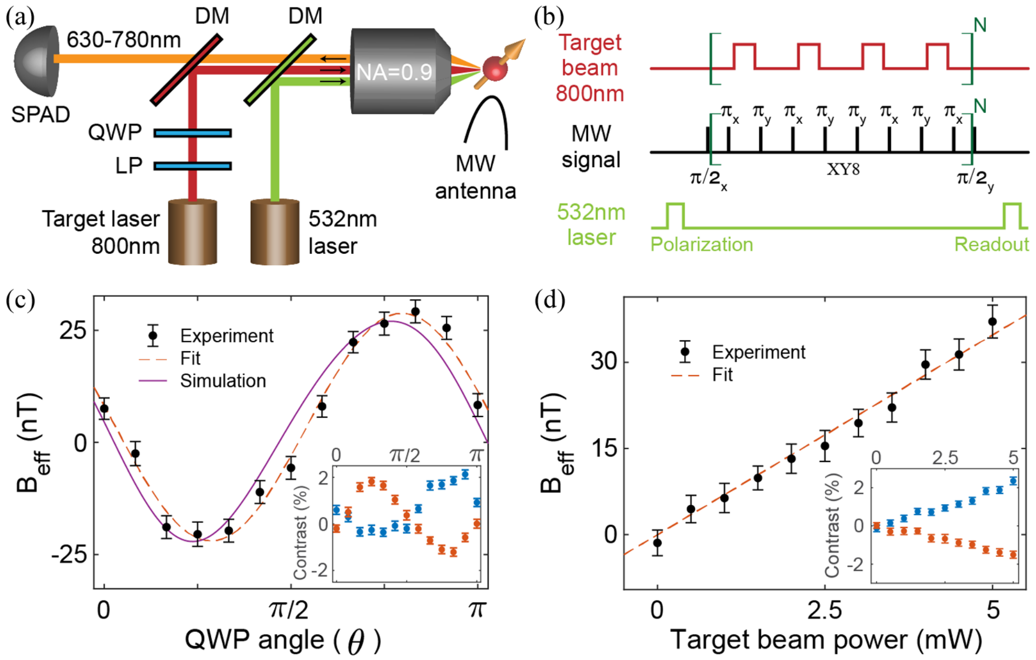

FIG. 4. Demonstration of nanoscale PSD probe with a single NV center. (a) Simplified schematic of the experimental setup. (b) Pulse sequence showing dynamical decoupling for ac magnetometry and amplitude modulation of the target beam to generate an ac effective magnetic field suitable for high sensitivity measurement. (c) Measured PSD for different QWP angles with target beam power of 4 mW. The dashed red curve is a sine fit to the data, the solid purple curve is the numerical simulation results, matching closely to the measurements. (d) Measured PSD as a function of incident power for $\theta = 3\pi/4$ showing a linear dependence. The dashed red curve is a linear fit. Insets show the raw measurement data for $|0\rangle \to |+1\rangle$ (red) and $|0\rangle \to |-1\rangle$ (blue) transitions. Panels (c) and (d) show that the effective field is directly proportional to PSD.

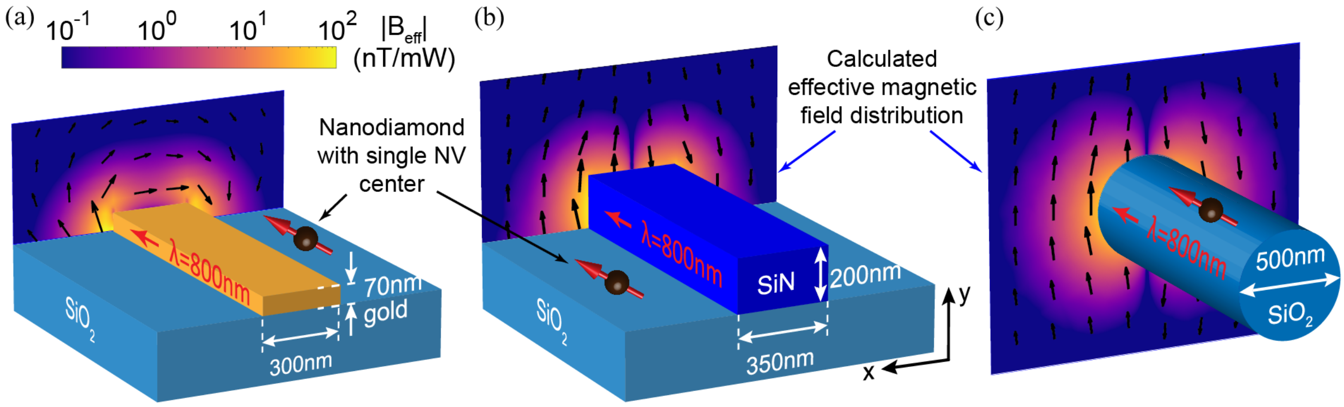

FIG. 5. Effective static magnetic field sensed by an NV center near optical waveguides. Our rigorous simulations are performed using full wave analysis of the optical fields along with the light-matter interaction theory of Sec. 1. A plasmonic waveguide (a), a ridge waveguide (b), and an optical fiber (c) all producing transverse effective static magnetic fields due to the PSD of their evanescent fields. The direction of the effective static magnetic field is shown with black arrows and its amplitude with the colormap. The mode of the ridge waveguide is transverse electric (TE) and the mode of the optical fiber is $\hat{x}$ polarized HE_{11}.

interaction of PSD with NV centers and is a synthetic magnetic field. PSD-induced effective static magnetic fields can produce giant spatial gradients on the order of 10 T/m with an ultrafast temporal response [42]. This allows for on-chip and targeted nanoscale addressing of spin qubits. Figure 5 shows the effective static magnetic field in the near-field region of a plasmonic waveguide, a ridge waveguide, and an optical fiber. This effective static magnetic field originates solely from the PSD of the evanescent waves in the vicinity of the waveguides. The direction of the field is in the x-y plane and is shown with black arrows. All three cases show short-range effective static magnetic field suitable for addressing single NV centers on chip or deposited on the surface of an optical fiber. This phenomenon opens the door to dense integration of single spin qubits for on-chip spin QED applications.

V. CONCLUSIONS

In this paper, we have demonstrated a room-temperature quantum probe for nanoscale spinning light fields. The spinning optical beam induces a magnetic field in the spin qubit causing a qubit rotation on the Bloch sphere (phase accumulation). The ultra-sub-wavelength behavior of spin angular momentum possess unique challenges for direct observation which we overcome using state of the art quantum sensing approaches. Our measurement reveals that the NV center's room-temperature excited-state energy levels display striking agreement with those found in low-temperature measurements. This is in contrast to direct measurements on the excited state where its full features cannot be revealed due to time averaging [43,44]. Our work can lead to new spin-dependent topological phases of light and also presents a way to exploit the universal resource of spinning evanescent waves available on an integrated photonics platform.

ACKNOWLEDGMENTS

Authors acknowledge funding from DARPA Nascent Light-Matter Interactions. The authors thank Ashwin Boddeti and Mahdi Hosseini for helpful discussions. L.P.Y. is also supported by the funding from Ministry of Science and Technology of China (Grant No. 2021YFE0193500). Leif Bauer acknowledges the National Science Foundation for support under the Graduate Research Fellowship Program (GRFP) under Grant No. DGE-1842166.

APPENDIX A: CALCULATIONS FOR PHOTONIC SPIN DENSITY-INDUCED EFFECTIVE STATIC MAGNETIC FIELD

We now show how to calculate the effective static magnetic field induced by far off-resonant electric dipole transitions. Virtual electric dipole transitions will induce energy shifts in the ground states, which can be described by an effective Hamiltonian $H_{\mathrm{shift}} = \sum_i \delta_i |i\rangle\langle i|$ with the shift [30,37],

$$\delta_i = \frac{1}{4\hbar^2} \sum_f \frac{|\langle f|\vec{d}|i\rangle \cdot \vec{E}(\vec{r},t)|^2}{\Delta_{\mathrm{if}} + \Gamma_f^2/4\Delta_{\mathrm{if}}}. \tag{A1}$$

Here $|i\rangle$ and $|f\rangle$ are the initial and final states of the possible transitions in an NV center as shown in Fig. 6, Δ_{ij} is the difference between the center frequency of the off-resonant excitation (ω_0) and the resonance frequency of the transition (ω_{ij}), Γ_f is the spontaneous decay rate of the final state, and $\vec{E}(\vec{r},t)$ is the electric field of the excitation at the position of the NV ($\vec{r}$). Usually, the detuning is much larger than the spontaneous decay rate. Thus, the Γ_f^2 term will be neglected. We show that the energy difference in the states $\{|0\rangle, |\pm 1\rangle\}$ induced by the off-resonance light functions as an effective static magnetic field for the NV ground-state spin.

1. Energy structure of NV center

To calculate this effective static magnetic field, we first give the eigenenergy spectrum and the possible transitions in the NV center. We only consider the six triplet excited states and neglect the other singlet states [35,36], as the electric dipole transitions do not change spin states. For convenience, we

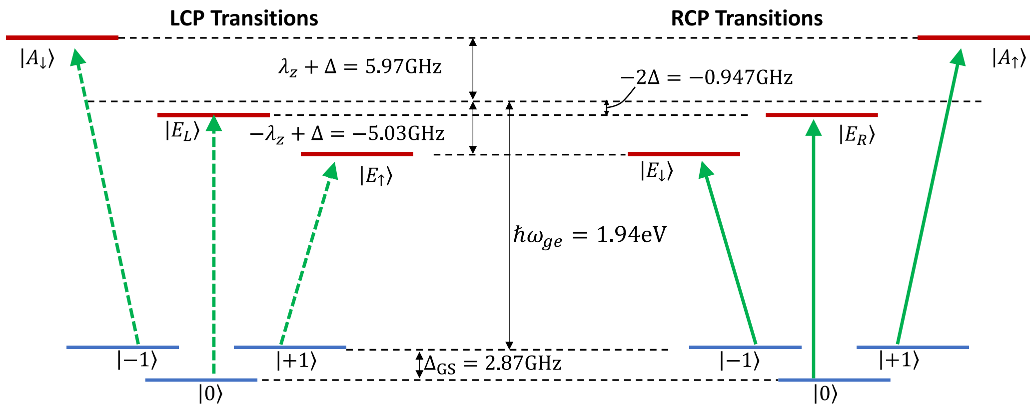

FIG. 6. Schematic of energy levels of the NV center. Here, there are no external magnetic field and strain. Left and right panels show the possible transitions induced by left circularly polarized (LCP) and right circularly polarized (RCP) lights.

choose a basis set, which is both spin- and orbital angular momentum resolved:

$$\begin{aligned}
|E_L\rangle &= \frac{1}{\sqrt{2}}(|E_y\rangle - i|E_x\rangle)\\
&= \frac{i}{2}[|a_1\rangle|e_+\rangle - |e_+\rangle|a_1\rangle] \otimes (|\uparrow\downarrow\rangle + |\downarrow\uparrow\rangle), \qquad \text{(A2)}
\end{aligned}$$

$$\begin{aligned}
|E_R\rangle &= \frac{1}{\sqrt{2}}(|E_y\rangle + i|E_x\rangle)\\
&= \frac{i}{2}[|a_1\rangle|e_-\rangle - |e_-\rangle|a_1\rangle] \otimes (|\uparrow\downarrow\rangle + |\downarrow\uparrow\rangle), \qquad \text{(A3)}
\end{aligned}$$

$$\begin{aligned}
|E_\downarrow\rangle &= \frac{1}{\sqrt{2}}(|E_2\rangle + |E_1\rangle)\\
&= \frac{1}{\sqrt{2}}(|a_1\rangle|e_-\rangle - |e_-\rangle|a_1\rangle) \otimes |\downarrow\downarrow\rangle, \qquad \text{(A4)}
\end{aligned}$$

$$\begin{aligned}
|E_\uparrow\rangle &= \frac{1}{\sqrt{2}}(|E_2\rangle - |E_1\rangle)\\
&= \frac{1}{\sqrt{2}}(|a_1\rangle|e_+\rangle - |e_+\rangle|a_1\rangle) \otimes |\uparrow\uparrow\rangle, \qquad \text{(A5)}
\end{aligned}$$

$$\begin{aligned}
|A_\uparrow\rangle &= \frac{1}{\sqrt{2}}(|A_2\rangle + |A_1\rangle)\\
&= \frac{1}{\sqrt{2}}(|a_1\rangle|e_-\rangle - |e_-\rangle|a_1\rangle) \otimes |\uparrow\uparrow\rangle, \qquad \text{(A6)}
\end{aligned}$$

$$\begin{aligned}
|A_\downarrow\rangle &= \frac{1}{\sqrt{2}}(|A_2\rangle - |A_1\rangle)\\
&= \frac{1}{\sqrt{2}}(|a_1\rangle|e_+\rangle - |e_+\rangle|a_1\rangle) \otimes |\downarrow\downarrow\rangle, \qquad \text{(A7)}
\end{aligned}$$

where $|a_1\rangle$, $|e_x\rangle$, and $|e_y\rangle$ are the orbital states of the NV center and $|e_\pm\rangle = \mp(|e_x\rangle \pm i|e_y\rangle)/\sqrt{2}$.

The ground states are given by

$$|-1\rangle = \frac{1}{\sqrt{2}}(|e_x e_y\rangle - |e_y e_x\rangle) \otimes |\downarrow\downarrow\rangle, \qquad \text{(A8)}$$

$$|0\rangle = \frac{1}{2}(|e_x e_y\rangle - |e_y e_x\rangle) \otimes (|\uparrow\downarrow\rangle + |\downarrow\uparrow\rangle), \qquad \text{(A9)}$$

$$|+1\rangle = \frac{1}{\sqrt{2}}(|e_x e_y\rangle - |e_y e_x\rangle) \otimes |\uparrow\uparrow\rangle. \qquad \text{(A10)}$$

We note that this normalization is different from Refs. [35,36]. The possible electric dipole transition are shown in Fig. 6.

The effective excited-state Hamiltonian of the NV center is given by Eq. (1). The optical gap $\hbar\omega_{\mathrm{ge}} \approx 1.945$ eV (637 nm) between the ground states and the excited states (see Fig. 6) has not been shown in H_{ES}. The off-diagonal coupling between these six excited states does not change this virtual transition-induced effective static magnetic field. Thus, we have omitted those off-diagonal coupling terms and the excited-state Hamiltonian is of diagonal form $H_{\mathrm{ES}} = E_j|j\rangle\langle j|$ where $|j\rangle \in \{|A_\uparrow\rangle, |A_\downarrow\rangle, |E_R\rangle, |E_L\rangle, |E_\uparrow\rangle, |E_\downarrow\rangle\}$.

2. Energy shifts and effective magnetic field for the ground-state spin

We now also give the transition elements of the electric dipole transitions in the NV center. As the upper basis is based on the two-hole picture, the electric dipole operator of the NV is given by

$$\vec{d} = e(\vec{r}_1 + \vec{r}_2), \qquad \text{(A11)}$$

where $\vec{r}_1$ and $\vec{r}_2$ are the position operator of the two holes. According to the symmetry of the orbits shown in [36], the nonzero elements of the dipolar transitions are

$$e\langle e_x|r_x|e_x\rangle = -e\langle e_y|r_y|e_y\rangle = e\langle e_y|r_y|e_x\rangle \neq 0. \qquad \text{(A12)}$$

and

$$e\langle a_1|r_x|e_x\rangle = e\langle a_1|r_y|e_y\rangle \equiv d_0 \neq 0. \qquad \text{(A13)}$$

The possible transitions and the corresponding transition strength can be easily obtained by the transition element. The nonzero transition elements are follows:

$$\langle E_L|\vec{d}|0\rangle = d_0\vec{e}_R,\ \langle E_R|\vec{d}|0\rangle = d_0\vec{e}_L, \qquad \text{(A14)}$$

$$\langle A_\uparrow|\vec{d}|+1\rangle = id_0\vec{e}_L,\ \langle E_\uparrow|\vec{d}|+1\rangle = id_0\vec{e}_R \qquad \text{(A15)}$$

$$\langle A_\downarrow|\vec{d}|-1\rangle = id_0\vec{e}_R,\ \langle E_\downarrow|\vec{d}|-1\rangle = id_0\vec{e}_L, \qquad \text{(A16)}$$

where we have defined the unit vectors

$$\vec{e}_L = (\vec{e}_x + i\vec{e}_y)/\sqrt{2},\ \vec{e}_R = (\vec{e}_x - i\vec{e}_y)/\sqrt{2}. \qquad \text{(A17)}$$

TABLE II. Selection rules for optical transitions between the triplet ground states and the triplet excited states. We note that any transition connected with circularly polarized light can also be stimulated with linearly polarized lights. But the corresponding transition strength will be smaller.

Polarization	$\vert A_\uparrow\rangle$	$\vert A_\downarrow\rangle$	$\vert E_R\rangle$	$\vert E_L\rangle$	$\vert E_\uparrow\rangle$	$\vert E_\downarrow\rangle$
$\vert -1\rangle$		LCP				RCP
$\vert 0\rangle$			RCP	LCP		
$\vert +1\rangle$	RCP				LCP	

Using the identities of the unit vectors $\vec{e}_R \cdot \vec{e}_R^* = \vec{e}_R \cdot \vec{e}_L = 1$ and $\vec{e}_R \cdot \vec{e}_R = \vec{e}_L \cdot \vec{e}_L = 0$, one can easily obtain the selection rules in Table II.

The value of the transition element can be obtained from the life times of the triplet excited states:

$$\tau_{\mathrm{NV}} = \frac{1}{\gamma_{\mathrm{NV}}} \approx \left(\frac{\omega_{eg}^3 d_0^2}{3\pi\hbar\varepsilon_0 c^3} \right)^{-1}. \tag{A18}$$

In this work, the lifetime of the NV center is taken as $\tau_{\mathrm{NV}} = 15$ ns. Then we have $d_0 \approx 2.485 \times 10^{-29}$ C m.

For simplicity, we first consider the case where the NV center axis is aligned with the propagating direction of the off-resonant excitation $(+\hat{z})$. The energy shifts in the ground states sub-levels under a LCP or RCP excitation field are given by

$$\delta_{-1,L} = \frac{1}{4\hbar^2} \frac{d_0^2 \Delta_{-1,A_\downarrow}}{\Delta_{-1,A_\downarrow}^2 + \Gamma^2/4} |\vec{E}(\vec{r})|^2,$$

$$\delta_{-1,R} = \frac{1}{4\hbar^2} \frac{d_0^2 \Delta_{-1,E_\downarrow}}{\Delta_{-1,E_\downarrow}^2 + \Gamma^2/4} |\vec{E}(\vec{r})|^2, \tag{A19}$$

$$\delta_{0,L} = \frac{1}{4\hbar^2} \frac{d_0^2 \Delta_{0,E_L}}{\Delta_{0,E_L}^2 + \Gamma^2/4} |\vec{E}(\vec{r})|^2,$$

$$\delta_{0,R} = \frac{1}{4\hbar^2} \frac{d_0^2 \Delta_{0,E_R}}{\Delta_{0,E_R}^2 + \Gamma^2/4} |\vec{E}(\vec{r})|^2, \tag{A20}$$

$$\delta_{+1,L} = \frac{1}{4\hbar^2} \frac{d_0^2 \Delta_{+1,E_\uparrow}}{\Delta_{+1,E_\uparrow}^2 + \Gamma^2/4} |\vec{E}(\vec{r})|^2,$$

$$\delta_{+1,R} = \frac{1}{4\hbar^2} \frac{d_0^2 \Delta_{+1,A_\uparrow}}{\Delta_{+1,A_\uparrow}^2 + \Gamma^2/4} |\vec{E}(\vec{r})|^2. \tag{A21}$$

where the detunings are given by

$$\Delta_{-1,j} = \omega_0 - (\omega_{\mathrm{ge}} + E_j + \gamma_{\mathrm{NV}} B), \tag{A22}$$

$$\Delta_{0,j} = \omega_0 - (\omega_{\mathrm{ge}} + E_j + \Delta_{\mathrm{GS}}), \tag{A23}$$

$$\Delta_{+1,j} = \omega_0 - (\omega_{\mathrm{ge}} + E_j - \gamma_{\mathrm{NV}} B). \tag{A24}$$

3. Effective static magnetic field for probe qubits

In the experiment, we choose two ground states sub-levels to form a qubit to detect the relative energy shift between them. The effective static magnetic fields for the three possible qubits are defined as

$$B_{01,L} = \frac{\delta_{+1,L} - \delta_{0,L}}{\gamma_{\mathrm{NV}}}, \quad B_{01,R} = \frac{\delta_{+1,R} - \delta_{0,R}}{\gamma_{\mathrm{NV}}}, \tag{A25}$$

$$B_{-10,L} = \frac{\delta_{0,L} - \delta_{-1,L}}{\gamma_{\mathrm{NV}}}, \quad B_{-10,R} = \frac{\delta_{0,R} - \delta_{-1,R}}{\gamma_{\mathrm{NV}}} \tag{A26}$$

$$B_{-11,L} = \frac{\delta_{+1,L} - \delta_{-1,L}}{2\gamma_{\mathrm{NV}}}, \quad B_{-11,R} = \frac{\delta_{+1,R} - \delta_{-1,R}}{2\gamma_{\mathrm{NV}}}. \tag{A27}$$

We note that the amplitude of the effective static magnetic field is linearly proportional to the off-resonant laser power. We can also tune the effective magnetic field via changing the polarization of the laser. The polarization unit vector of an arbitrary polarized light can be expanded as

$$\vec{e} = \vec{e}_L \cos\left(\theta - \frac{\pi}{4}\right) + \vec{e}_R \sin\left(\theta - \frac{\pi}{4}\right), \tag{A28}$$

where the angle $\theta \in [0, 2\pi)$ is the rotation angle of a QWP. In addition, in the experiment the NV center axis makes an angle ϕ with the propagating direction of the off-resonant beam. We need to transform the LCP and RCP unit vectors in the NV center coordinate frame $(x'y'z')$ into the excitation beam coordinate frame (xyz) as shown in Fig. 7,

$$\vec{e}_L' = \frac{1}{2}\vec{e}_L(\cos\phi + 1) + \frac{1}{2}\vec{e}_R(\cos\phi - 1) + \frac{1}{\sqrt{2}}\vec{e}_z \sin\phi, \tag{A29}$$

$$\vec{e}_R' = \frac{1}{2}\vec{e}_R(\cos\phi + 1) + \frac{1}{2}\vec{e}_L(\cos\phi - 1) + \frac{1}{\sqrt{2}}\vec{e}_z \sin\phi. \tag{A30}$$

In this case, the three effective magnetic fields are given by

$$B_{01} = B_{01,L}|\vec{e} \cdot \vec{e}_L'^*|^2 + B_{01,R}|\vec{e} \cdot \vec{e}_R'^*|^2, \tag{A31}$$

$$B_{-10} = B_{-10,L}|\vec{e} \cdot \vec{e}_L'^*|^2 + B_{-10,R}|\vec{e} \cdot \vec{e}_R'^*|^2, \tag{A32}$$

$$B_{-11} = B_{-11,L}|\vec{e} \cdot \vec{e}_L'^*|^2 + B_{-11,R}|\vec{e} \cdot \vec{e}_R'^*|^2. \tag{A33}$$

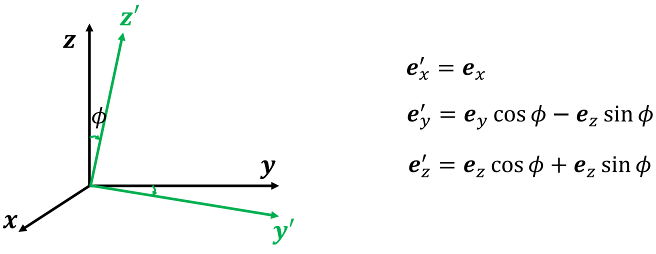

FIG. 7. Transformation between the NV center coordinate frame and the off-resonant beam coordinate frame.

Using the fact that $\delta_{-1,L} = \delta_{+1,R}$ and $\delta_{-1,R} = \delta_{+1,L}$, we can rewrite B_{-11} as

$$B_{-11} = \frac{\delta_{+1,L} - \delta_{+1,R}}{2\gamma_{\rm NV}|\vec{E}(\vec{r})|^2}\{-i[\vec{E}^*(\vec{r}) \times \vec{E}(\vec{r})] \cdot \vec{n}\} \tag{A34}$$

$$= \frac{\omega_0(\delta_{+1,L} - \delta_{+1,R})}{\epsilon\gamma_{\rm NV}|\vec{E}(\vec{r})|^2}\{\vec{S} \cdot \vec{n}\} \tag{A35}$$

$$\approx -\frac{\omega_0 d_0^2 \lambda_z}{\hbar^2\epsilon\gamma_{\rm NV}\Delta_{+1,A_\uparrow}\Delta_{+1,E_\uparrow}}\{\vec{S} \cdot \vec{n}\}. \tag{A36}$$

Here ϵ is the permittivity of diamond, $\vec{S} = -(i\epsilon/4\omega_0)[\vec{E}^* \times \vec{E} + \vec{H}^* \times \vec{H}] = -(i\epsilon/2\omega_0)\vec{E}^* \times \vec{E}$ is the photonic spin density in the single-frequency limit, and $\hat{n}$ is the direction of the NV center. We have also used the relation,

$$\vec{e}^* \times \vec{e} = i\left[\cos^2\left(\theta - \frac{\pi}{4}\right) - \sin^2\left(\theta - \frac{\pi}{4}\right)\right]\vec{e}_z = i\sin(2\theta)\vec{e}_z. \tag{A37}$$

In the far off-resonant case $\Delta_{+1,A_\uparrow} \approx \Delta_{+1,E_\uparrow} = \Delta$. In this case the denominator is only determined by the frequency of the off-resonant beam and the spin-orbit coupling factor in the excited state. $B_{\rm eff}$ can be written in the following form:

$$B_{\rm eff} = B_{-11} = -\frac{\omega_0 d_0^2 \lambda_z}{\hbar^2\epsilon\gamma_{\rm NV}\Delta^2}(\vec{S}_E \cdot \vec{n}) = C(\vec{S}_E \cdot \vec{n}) \tag{A38}$$

where C is a constant.

APPENDIX B: INFLUENCE OF COUPLING BETWEEN NV CENTER'S EXCITED-STATE SUBLEVELS ON THE EFFECTIVE STATIC MAGNETIC FIELD

In this subsection, we show that the off-diagonal coupling in the excited-state sublevels will not affect the effective static magnetic field. The full Hamiltonian for the excited state of the NV center in the set of basis $\{|A_\uparrow\rangle, |A_\downarrow\rangle, |E_R\rangle, |E_L\rangle, |E_\uparrow\rangle, |E_\downarrow\rangle\}$ is given by [36],

$$H_{\rm ES} = \begin{bmatrix} \gamma_{\rm NV}B+\Delta_{\rm es}+\lambda_z & \zeta' & 0 & 0 & -(\eta_1+i\eta_2) & 0 \\ \zeta' & -\gamma_{\rm NV}B+\Delta_{\rm es}+\lambda_z & 0 & 0 & 0 & -(\eta_1-i\eta_2) \\ 0 & 0 & -2\Delta_{\rm es} & -(\eta_1+i\eta_2) & 0 & -\zeta'' \\ 0 & 0 & -(\eta_1-i\eta_2) & -2\Delta_{\rm es} & \zeta'' & 0 \\ -(\eta_1-i\eta_2) & 0 & 0 & \zeta'' & \gamma_{\rm NV}B+\Delta_{\rm es}-\lambda_z & 0 \\ 0 & -(\eta_1+i\eta_2) & -\zeta'' & 0 & 0 & -\gamma_{\rm NV}B+\Delta_{\rm es}-\lambda_z \end{bmatrix}, \tag{B1}$$

where ζ' and ζ'' are the spin-spin-induced off-diagonal zero-field splitting (ZFS). In an experiment, we can easily tune the Zeeman splitting with an external magnetic field. The strain η_1, η_2 can also be tuned by adding an electric field. These off-diagonal terms have been neglected in Eq. (1) because they do not change the effective static magnetic field induced by PSD as we show in this subsection.

For a given set of parameters, we can diagonalize the Hamiltonian (B1) to obtain the eigenstates and the corresponding eigenvalues:

$$H_{\rm ES}|m\rangle = E_m|m\rangle, m = 1, \ldots, 6. \tag{B2}$$

Here, we only take the effective static magnetic field induced by an RCP light as an example. The energy shifts in the ground-state sublevels are given by

$$\delta_{-1,R} = \frac{d_0^2}{4\hbar^2}\sum_m \frac{\langle E_\downarrow|m\rangle\langle m|E_\downarrow\rangle\Delta_{-1,m}}{\Delta_{-1,m}^2 + \Gamma^2/4}|\vec{E}(\vec{r})|^2, \tag{B3}$$

$$\delta_{0,R} = \frac{d_0^2}{4\hbar^2}\sum_m \frac{\langle E_R|m\rangle\langle m|E_R\rangle\Delta_{0,m}}{\Delta_{0,m}^2 + \Gamma^2/4}|\vec{E}(\vec{r})|^2, \tag{B4}$$

$$\delta_{+1,R} = \frac{d_0^2}{4\hbar^2}\sum_m \frac{\langle A_\uparrow|m\rangle\langle m|A_\uparrow\rangle\Delta_{+1,m}}{\Delta_{+1,m}^2 + \Gamma^2/4}|\vec{E}(\vec{r})|^2, \tag{B5}$$

where

$$\Delta_{-1,m} = \omega_0 - (\omega_{\rm ge} + E_m + \gamma_{\rm NV}B), \tag{B6}$$

$$\Delta_{0,m} = \omega_0 - (\omega_{\rm ge} + E_m + \Delta_{\rm GS}), \tag{B7}$$

$$\Delta_{+1,m} = \omega_0 - (\omega_{\rm ge} + E_m - \gamma_{\rm NV}B). \tag{B8}$$

The effective static magnetic field can be defined via Eqs. (A25)–(A27).

In the case of applying a far off-resonant beam with center wavelength $\lambda_0 = 800$ nm, an NV center is not pumped to the excited state. As shown in Fig. 8(a), the effective static magnetic field $B_{\rm eff}$ induced by a circularly polarized light is almost independent of the amplitude of the off-diagonal ZFS terms, ζ'' and ζ'', which mix the excited-state sublevels. In Fig. 8(b), we show that in the far off-resonant case, the effective static magnetic field $B_{\rm eff}$ is also independent of the external magnetic field and strain η.

In this subsection we showed numerically that coupling between the excited-state sublevels does not change the energy shift experienced by the ground-state energy levels due to a far off-resonant excitation. A similar argument also applies to the dynamic Jahn-Teller effect in the NV center's electronic excited states [45]. Therefore, it is possible to measured a PSD dependent effective static magnetic field while resolving NV center's excited-state energy levels at room temperature is not possible.

APPENDIX C: EXPERIMENTAL SETUP

A schematic of the experimental setup is shown in Fig. 9(a). The setup comprises an NV center and three main beam paths. The NV center [Fig. 9(b)] is on an AFM tip and is implanted 10 nm deep into the surface of the tip. The tip is purchased from QZabre LLC. The second-order correlation measurement for the single NV center is shown in Fig. 9(b). A magnet breaks the degeneracy of $|\pm 1\rangle$ states by applying a magnetic field $B_{\rm bias} \approx 1.1$ mT. An antenna made of a 15-μm-

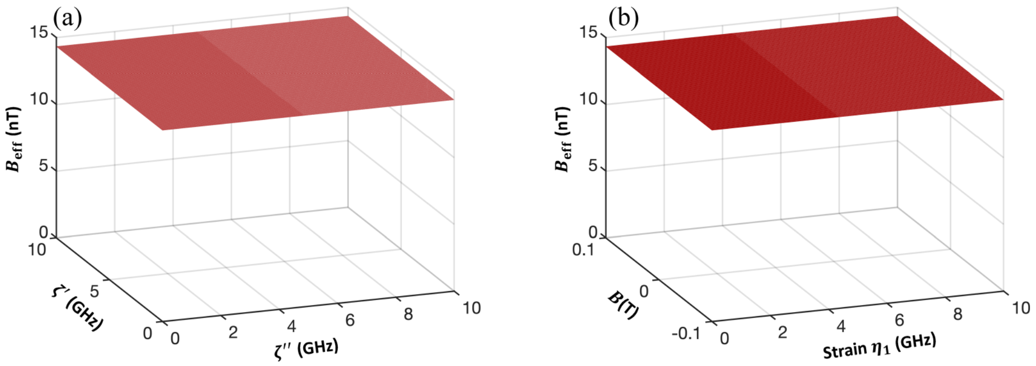

FIG. 8. (a) The effective static magnetic field B_{eff} experienced by the qubit formed by $|-1\rangle$ and $|+1\rangle$ as a function of spin-spin-induced zero-field splitting ζ' and ζ''. (b) The effective static magnetic field B_{eff} as a function of the external magnetic field B and the strain η_1. Here, the other parameters are taken as $\lambda_z/2\pi = 5.5$ GHz, $\Delta_{\mathrm{es}}/2\pi = 1.42/3$ GHz, the center wavelength of the right-handed circularly polarized excitation is $\lambda_0 = 800$ with laser power 1 mW.

thick tungsten wire delivers a MW signal to the NV center to induce Rabi oscillations [Fig. 9(c)].

A 532-nm laser is used for excitation and readout of the state of the NV center. The beam is chopped with an AOM for pulsed measurements. After the linear polarizer the beam is coupled to a polarization maintaining (PM) fiber. The output of the fiber is collimated and filtered with a band-pass filter (BPF) (Thorlabs FLH532-10).

The target laser is a TTL controlled laser diode module (Power Technology Inc. PMT150). The beam is coupled into a PM fiber after a linear polarizer. The output of the fiber is collimated and goes through a quarter-wave plate before being filtered with a BPF (FBH800-10). Due to reflection from a dichroic mirror, the polarization of the beam has an ellipticity of $\varepsilon = 1.08$ before entering the objective lens when the QWP is at its optimal angle.

The photoluminescence signal from the NV center is filtered with a long-pass filter (Semrock BLP02-561-R), a short-pass filter (Semrock SP01-785RU), and a BPF (Semrock FF01-709/167). Three dichroic mirrors (DM) combine

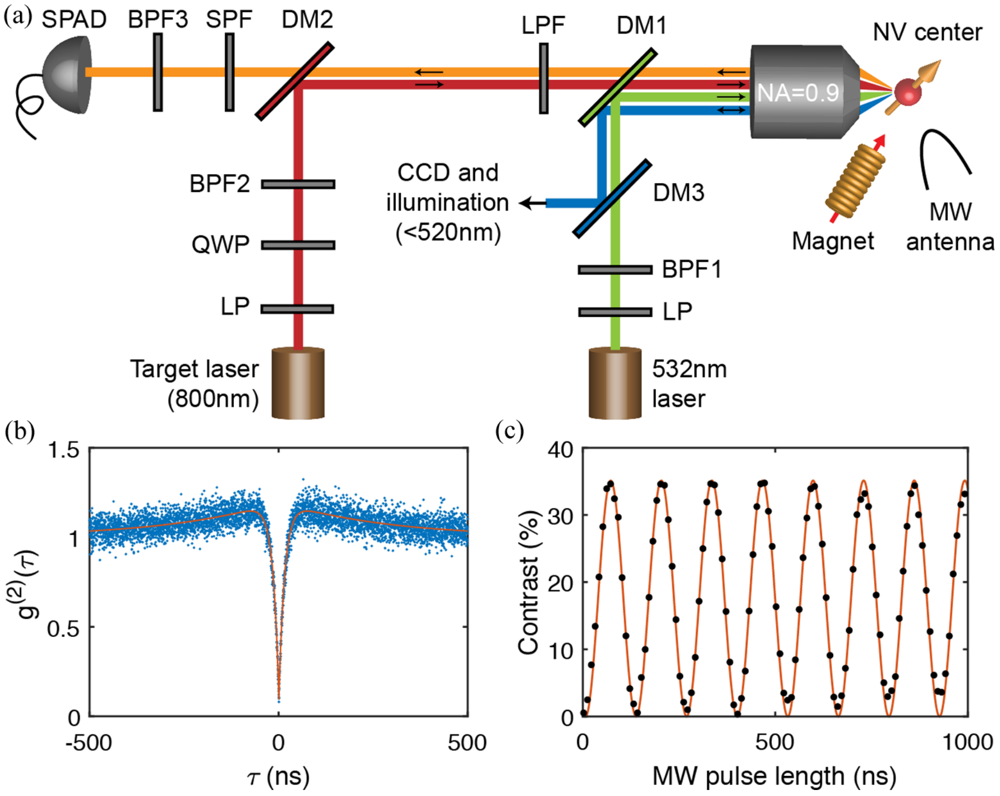

FIG. 9. Schematic of the experimental setup. (a) Schematic of the setup showing the beam paths and filters. (b) Second-order correlation measurement showing that the AFM tip contains a single NV center. (c) Rabi oscillations showing the interaction of the microwave beam (MW) with the NV center. LP, linear polarizer; DM, dichroic mirror; BPF, band-pass filter; LPF, long-pass filter; SPF, short-pass filter; QWP, quarter-wave plate.

and separate the beams; DM1, Thorlabs DMLP550R; DM2, Semrock FF750-SDi02; DM3, Semrock FF520-Di02. The PL signal is detected by a Micro Photon Devices SPAD. For measuring $g^{(2)}$ the signal is coupled to a fiber optic beam splitter and is detected with two SPADs.

APPENDIX D: PULSE SEQUENCE

Here we will explain how the measurement is performed in details. Depending on which transition the MW field is resonant to ($|0\rangle$ to $|+1\rangle$ or $|0\rangle$ to $|-1\rangle$) we choose those two states as a two-level system. The pulse sequence shown in Fig. 3 starts with initializing the NV center in $|0\rangle$ state. Then a series of π and $\pi/2$ pulses manipulate the state of the NV center to prepare the NV center for interaction and readout and to increase the coherence time. The state after each pulse is calculated using the following rotation matrices,

$$R_x(\theta) = \begin{bmatrix} \cos\frac{\theta}{2} & -i\sin\frac{\theta}{2} \\ -i\sin\frac{\theta}{2} & \cos\frac{\theta}{2} \end{bmatrix}$$

$$\text{and} \quad R_y(\theta) = \begin{bmatrix} \cos\frac{\theta}{2} & -\sin\frac{\theta}{2} \\ \sin\frac{\theta}{2} & \cos\frac{\theta}{2} \end{bmatrix},$$

where $\theta = \pi/2$ ($\theta = \pi$) for $\pi/2$ pulse (π pulse).

We show the calculations for $|0\rangle$ to $|+1\rangle$ transition here. The sequence starts with initializing the NV center into $|0\rangle$ state. Then a $\pi/2$ pulse rotates the spin into a superposition state and a series of π pulses perform the dynamical decoupling while the target beam affects the state of the NV center. The effect of each pulse of the target beam is captured by an added phase, ϕ. We are assuming that the MW pulses are very short and off-resonant to the NV center by $\omega - \omega_0 = \delta\omega$. This adds a phase $\Theta = \delta\omega\tau/2$ during each free procession period of length $\tau/2$. In our experiment we omit the first and last half target pulses in measurement 1 and omit the last target pulse in measurement 2 for simplicity. Therefore, each measurement contains total of $4N - 1$ target pulses, where N is the number of XY8 pulses.

After sending N number of XY8 pulses, a total of 8N π-pulses have been sent. The state of the NV center before the last $\pi/2$ pulse is

$$|\psi(N\tau)\rangle = \frac{\sqrt{2}}{2}\left(e^{-i(4N-1)\phi}|0\rangle - ie^{i(4N-1)\phi}|+1\rangle\right),$$

We set the last $\pi/2$ pulse in the $-\hat{y}$ direction. The state of the NV center after this pulse is

$$|\psi(N\tau)\rangle = e^{-i\pi/4}(\cos(\pi/4 - \Phi)|0\rangle - i\sin(\pi/4 - \Phi)|+1\rangle), \tag{D1}$$

where $\Phi = (4N - 1)\phi$ is the total phase induced by the target beam. Measured contrast for this state, C_1, is

$$C_1 = C^{\max}|\langle\pm1|\psi\rangle|^2 = \sin^2(\pi/4 - \Phi)C^{\max}, \tag{D2}$$

where $C^{\max}$ is the contrast measured for $|\pm1\rangle$ states.

The outcome of Measurement 2 similarly will be

$$C_2 = \sin^2(\pi/4 + \Phi)C^{\max}, \tag{D3}$$

where the difference in the sign of Φ is due to the target pulses being sent in the opposite time slots. We calculate the phase Φ by subtracting the outcome of the two measurements,

$$\begin{aligned} C = C_1 - C_2 &= \frac{C^{\max}}{2}[\cos(\pi/2 + 2\Phi) - \cos(\pi/2 - 2\Phi)] \\ &= -\sin(2\Phi)C^{\max}. \end{aligned} \tag{D4}$$

In this approach, any undesired effect caused by adding the target beam (e.g., change of temperature and coherence) will be eliminated in the subtraction.

To measure $C^{\max}$, we employ the following procedure to ensure all the effects decreasing the coherence of the quantum states are accounted for. First we calculate the contrast C^{ave} for the state $|\psi\rangle = e^{-i\pi/4}(|0\rangle - i|+1\rangle)/\sqrt{2}$. Based on the measurements performed, $C^{\text{ave}} = (C_1 + C_2)/2$. Then we measure the contrast C^{+1} for the state $|\psi\rangle = -i|+1\rangle$. This measurement is performed with a pulse sequence similar to Measurements 1 and 2 with the difference that the last $\pi/2$ pulse is in $\hat{x}$ direction. Moreover, the target pulses are sent during both time slots to cancel out the effect of each other. The length of the pulses are set to halve of the pulses in Measurements 1 and 2 to keep the average power reaching the NV center same as measurements 1 and 2. This way any decoherence added to the system due to presence of the target beam is accounted for in measuring C^{+1}. Then we have

$$C^{\max} = 2(C^{+1} - C^{\text{ave}}). \tag{D5}$$

If instead of the target pulses a magnetic field B parallel to the axis of the NV center was applied, then the measured contrast would have been,

$$C = \sin(2\Phi)C^{\max} = -\sin[(8N - 2)\phi]C^{\max}, \tag{D6}$$

where $\phi = \gamma B\tau'/2$. In this equation γ is the gyromagnetic ratio for the NV center, and τ' is the length of the target pulses. Therefore, we define an effective magnetic field equivalent to the effect caused by the target beam,

$$\begin{aligned} B^{\text{eff}} &= \frac{-1}{(4N - 1)\gamma\tau'}\sin^{-1}\left(\frac{C}{C^{\max}}\right), \\ &\approx \frac{-C}{(4N - 1)\gamma\tau' C^{\max}} \end{aligned} \tag{D7}$$

In our experiments, shown in Fig. 3 (main text), $\tau' = 1\ \mu$s and $N = 4$ is the number of XY8 pulses. For Fig. 3(c) $C^{\max}$ is measured for the two measurements as, $C^{\max}_{|0\rangle\to|-1\rangle} = 20.3\% \pm 0.6$ and $C^{\max}_{|0\rangle\to|+1\rangle} = 19.2\% \pm 0.9$. For Fig. 3(d) $C^{\max}$ is measured for the two measurements as, $C^{\max}_{|0\rangle\to|-1\rangle} = 20.2\% \pm 0.8$ and $C^{\max}_{|0\rangle\to|+1\rangle} = 19.1\% \pm 0.6$.

APPENDIX E: FULL-WAVE ANALYSIS OF PROPAGATION OF LIGHT IN AFM TIP

Numerical simulations presented in Fig. 4(c) and Fig. 5 are performed with CST Studio Suite. The detail of the simulation results shown in Fig. 4(c) is explained here. Figure 10(a) shows the normalized amplitude of the electric field in the structure. The structure is an AFM tip on a substrate both made of diamond. The dimensions of the tip are estimates provided by QZabre company for the AFM tip we purchased. The excitation is a beam with wavelength $\lambda_0 = 800$ nm and Numerical aperture $NA = 0.65$ which resembles the target beam in our experiment [46]. Similarly to the experimental

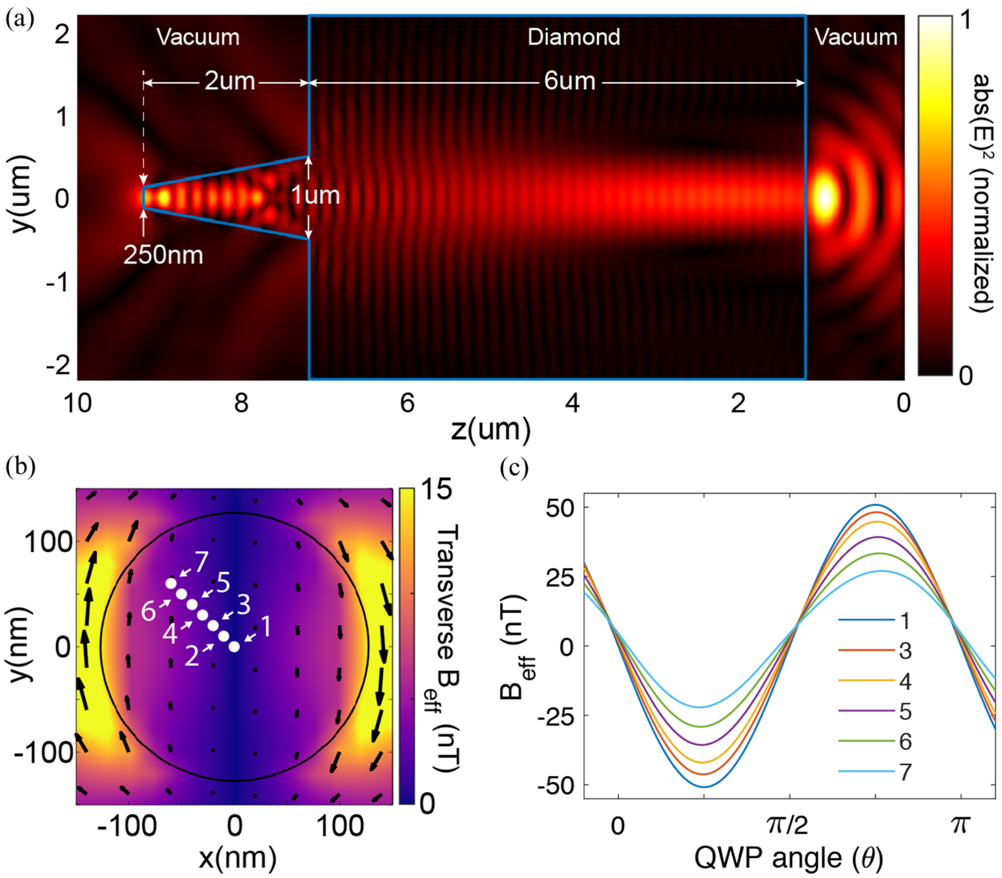

FIG. 10. Numerical simulations for the effective field amplitude in an AFM tip. (a) Amplitude of the electric field in an AFM tip made of diamond. (b) Amplitude and direction of the transverse component of the effective field in the plane of the NV center. (c) The effective field seen by an NV center with direction $\hat{n} = (\hat{x} + \hat{y} - \hat{z})/\sqrt{3}$ placed at various locations shown in panel (b) with white dots.

setup, the beam is x polarized before going through a QWP and travels through the fast axis of the wave plate when the wave plate angle (θ) is zero. Due to reflection of the target beam from a dichroic mirror in the experiment, the polarization of the beam has an ellipticity of $\varepsilon = 1.08$ before entering the objective lens when the QWP is at its optimal angle. However, this ellipticity is neglected in the simulations. The power of the beam is $P = 4$ mW before the objective lens which has a measured transmission of $T = 78\%$ at this wavelength. The power of the incident beam in the simulation is set to match this transmitted power in the experiment. The beam travels in $+\hat{z}$ direction and is focused at a distance $z_0 = 1.8$ μm if the medium was vacuum. The parameter z_0 is chosen such to qualitatively match the simulation results to the amplitude of the measured effective field.

Figure 10(b) shows the transverse effective field in the AFM tip in a plane 10 nm away from the end of the tip. This plane coincides with the depth of the implanted NV center. The black circle shows the circumference of the diamond tip in this plane. The colorbar shows the amplitude of the transverse field and the black arrows show its direction. This transverse field gives rise to the dc offset in the experimental result [Fig. 4(c)]. If the NV center is placed off-axes to the AFM tip there would be a nonzero transverse spin component at its location. This transverse component behaves differently from the longitudinal component of the photonic spin density when changing the QWP angle, giving rise to a dc offset.

To illustrate the effect of transverse spin, we show the effective magnetic field for an NV center in $\hat{n} = (\hat{x} + \hat{y} - \hat{z})/\sqrt{3}$ direction (same as the direction of the NV center in our experiment) placed at different locations on the transverse plane. Figure 10(c) shows the effective magnetic field along the direction of this NV center. Each curve corresponds to a different location for the NV center marked with white dots on Fig. 10(b). The dots have a relative distance of $d = -10nm\hat{x} + 10nm\hat{y}$ to each other. This figure clearly shows the development of the dc offset as the distance to the center of the tip increases. The Curve shown is Fig. 4(c) is the same as curve 7 in Fig. 10(c).

---

[1] T. van der Sar, F. Casola, R. Walsworth, and A. Yacoby, Nanometre-scale probing of spin waves using single electron spins, Nat. Commun. **6**, 7886 (2015).

[2] L. Thiel, Z. Wang, M. A. Tschudin, D. Rohner, I. Gutiérrez-Lezama, N. Ubrig, M. Gibertini, E. Giannini, A. F. Morpurgo, and P. Maletinsky, Probing magnetism in 2D materials at

the nanoscale with single-spin microscopy, Science **364**, 973 (2019).

[3] Y. Dovzhenko, F. Casola, S. Schlotter, T. X. Zhou, F. Büttner, R. L. Walsworth, G. S. D. Beach, and A. Yacoby, Magnetostatic twists in room-temperature skyrmions explored by nitrogen-vacancy center spin texture reconstruction, Nat. Commun. **9**, 2712 (2018).

[4] S. Kolkowitz, A. Safira, A. A. High, R. C. Devlin, S. Choi, Q. P. Unterreithmeier, D. Patterson, A. S. Zibrov, V. E. Manucharyan, H. Park, and M. D. Lukin, Probing Johnson noise and ballistic transport in normal metals with a single-spin qubit, Science **347**, 1129 (2015).

[5] J. A. Shockley and J. F. Raquet, Navigation of ground vehicles using magnetic field variations, Navigation **61**, 237 (2014).

[6] R. A. Beth, Mechanical detection and measurement of the angular momentum of light, Phys. Rev. **50**, 115 (1936).

[7] C. V. Raman and S. Bhagavantam, Experimental proof of the spin of the photon, Nature (London) **129**, 22 (1932).

[8] T. V. Mechelen and Z. Jacob, Universal spin-momentum locking of evanescent waves, Optica **3**, 118 (2016).

[9] K. Y. Bliokh, A. Y. Bekshaev, and F. Nori, Extraordinary momentum and spin in evanescent waves, Nat. Commun. **5**, 3300 (2014).

[10] K. Y. Bliokh, F. J. Rodríguez-Fortuño, F. Nori, and A. V. Zayats, Spinorbit interactions of light, Nat. Photon. **9**, 796 (2015).

[11] I. Shomroni, S. Rosenblum, Y. Lovsky, O. Bechler, G. Guendelman, and B. Dayan, All-optical routing of single photons by a one-atom switch controlled by a single photon, Science **345**, 903 (2014).

[12] X. Yin, P. Shi, L. Du, and X. Yuan, Spin-resolved near-field scanning optical microscopy for mapping of the spin angular momentum distribution of focused beams, Appl. Phys. Lett. **116**, 241107 (2020).

[13] L.-P. Yang and Z. Jacob, Quantum structured light: Non-classical spin texture of twisted single-photon pulses, arXiv:2102.13248 (2021).

[14] T. V. Mechelen and Z. Jacob, Photonic Dirac monopoles and skyrmions: Spin-1 quantization [Invited], Opt. Mater. Express **9**, 95 (2019).

[15] L. Du, A. Yang, A. V. Zayats, and X. Yuan, Deep-subwavelength features of photonic skyrmions in a confined electromagnetic field with orbital angular momentum, Nat. Phys. **15**, 650 (2019).

[16] S. Tsesses, E. Ostrovsky, K. Cohen, B. Gjonaj, N. H. Lindner, and G. Bartal, Optical skyrmion lattice in evanescent electromagnetic fields, Science **361**, 993 (2018).

[17] F. Kalhor, T. Thundat, and Z. Jacob, Universal spin-momentum locked optical forces, Appl. Phys. Lett. **108**, 061102 (2016).

[18] T. Zhang, M. R. C. Mahdy, Y. Liu, J. H. Teng, C. T. Lim, Z. Wang, and C.-W. Qiu, All-optical chirality-sensitive sorting via reversible lateral forces in interference fields, ACS Nano **11**, 4292 (2017).

[19] F. J. Rodríguez-Fortuño, N. Engheta, A. Martínez, and A. V. Zayats, Lateral forces on circularly polarizable particles near a surface, Nat. Commun. **6**, 8799 (2015).

[20] M. Neugebauer, T. Bauer, A. Aiello, and P. Banzer, Measuring the Transverse Spin Density of Light, Phys. Rev. Lett. **114**, 063901 (2015).

[21] A. Javadi, D. Ding, M. H. Appel, S. Mahmoodian, M. C. Löbl, I. Söllner, R. Schott, C. Papon, T. Pregnolato, S. Stobbe, L. Midolo, T. Schröder, A. D. Wieck, A. Ludwig, R. J. Warburton, and P. Lodahl, Spinphoton interface and spin-controlled photon switching in a nanobeam waveguide, Nat. Nanotechnol. **13**, 398 (2018).

[22] C. Sayrin, C. Junge, R. Mitsch, B. Albrecht, D. OShea, P. Schneeweiss, J. Volz, and A. Rauschenbeutel, Nanophotonic Optical Isolator Controlled by the Internal State of Cold Atoms, Phys. Rev. X **5**, 041036 (2015).

[23] A. V. Arzola, Lukáš Chvátal, Petr Jákl, and Pavel Zemánek, Spin to orbital light momentum conversion visualized by particle trajectory, Sci. Rep. **9**, 4127 (2019).

[24] S.-H. Gong, F. Alpeggiani, B. Sciacca, E. C. Garnett, and L. Kuipers, Nanoscale chiral valley-photon interface through optical spin-orbit coupling, Science **359**, 443 (2018).

[25] Z. Ji, W. Liu, S. Krylyuk, X. Fan, Z. Zhang, A. Pan, L. Feng, A. Davydov, and R. Agarwal, Photocurrent detection of the orbital angular momentum of light, Science **368**, 763 (2020).

[26] C. Cohen-Tannoudji, J. Dupont-Roc, and G. Grynberg, *Photons and Atoms—Introduction to Quantum Electrodynamics* (Wiley-VCH, New York, 1997).

[27] L.-P. Yang, F. Khosravi, and Z. Jacob, Quantum spin operator of the photon, arXiv:2004.03771 (2020).

[28] M. V. Berry, Optical currents, J. Opt. A: Pure Appl. Opt. **11**, 094001 (2009).

[29] M. F. Picardi, K. Y. Bliokh, F. J. Rodríguez-Fortuño, F. Alpeggiani, and F. Nori, Angular momenta, helicity, and other properties of dielectric-fiber and metallic-wire modes, Optica **5**, 1016 (2018).

[30] I. H. Deutsch and P. S. Jessen, Quantum-state control in optical lattices, Phys. Rev. A **57**, 1972 (1998).

[31] B. B. Buckley, G. D. Fuchs, L. C. Bassett, and D. D. Awschalom, Spin-light coherence for single-spin measurement and control in diamond, Science **330**, 1212 (2010).

[32] B. Albrecht, Y. Meng, C. Clausen, A. Dareau, P. Schneeweiss, and A. Rauschenbeutel, Fictitious magnetic-field gradients in optical microtraps as an experimental tool for interrogating and manipulating cold atoms, Phys. Rev. A **94**, 061401 (2016).

[33] T. A. Wilkinson, D. J. Cottrill, J. M. Cramlet, C. E. Maurer, C. J. Flood, A. S. Bracker, M. Yakes, D. Gammon, and E. B. Flagg, Spin-selective AC Stark shifts in a charged quantum dot, Appl. Phys. Lett. **114**, 133104 (2019).

[34] C. L. Degen, F. Reinhard, and P. Cappellaro, Quantum sensing, Rev. Mod. Phys. **89**, 035002 (2017).

[35] J. R. Maze, A. Gali, E. Togan, Y. Chu, A. Trifonov, E. Kaxiras, and M. D. Lukin, Properties of nitrogen-vacancy centers in diamond: The group theoretic approach, New J. Phys. **13**, 025025 (2011).

[36] Y. Chu and M. D. Lukin, *Quantum Optics with Nitrogen-vacancy Centers in Diamond* (Oxford University Press, Oxford, 2017).

[37] W. Happer and B. S. Mathur, Effective operator formalism in optical pumping, Phys. Rev. **163**, 12 (1967).

[38] M. W. Doherty, N. B. Manson, P. Delaney, F. Jelezko, J. Wrachtrup, and L. C. L. Hollenberg, The nitrogen-vacancy colour centre in diamond, Phys. Rep. **528**, 1 (2013).

[39] J. M. Taylor, P. Cappellaro, L. Childress, L. Jiang, D. Budker, P. R. Hemmer, A. Yacoby, R. Walsworth, and M. D. Lukin, High-sensitivity diamond magnetometer with nanoscale resolution, Nat. Phys. **4**, 810 (2008).

[40] M. A. Ali Ahmed, G. A. lvarez, and D. Suter, Robustness

of dynamical decoupling sequences, Phys. Rev. A **87**, 042309 (2013).

[41] V. M. Acosta, E. Bauch, M. P. Ledbetter, A. Waxman, L.-S. Bouchard, and D. Budker, Temperature Dependence of the Nitrogen-Vacancy Magnetic Resonance in Diamond, Phys. Rev. Lett. **104**, 070801 (2010).

[42] R. Mitsch, C. Sayrin, B. Albrecht, P. Schneeweiss, and A. Rauschenbeutel, Exploiting the local polarization of strongly confined light for sub-micrometer-resolution internal state preparation and manipulation of cold atoms, Phys. Rev. A **89**, 063829 (2014).

[43] P. Neumann, R. Kolesov, V. Jacques, J. Beck, J. Tisler, A. Batalov, L. Rogers, N. B. Manson, G. Balasubramanian, F. Jelezko, and J. Wrachtrup, Excited-state spectroscopy of single NV defects in diamond using optically detected magnetic resonance, New J. Phys. **11**, 013017 (2009).

[44] L. J. Rogers, R. L. McMurtrie, M. J. Sellars, and N. B. Manson, Time-averaging within the excited state of the nitrogen-vacancy centre in diamond, New J. Phys. **11**, 063007 (2009).

[45] T. A. Abtew, Y. Y. Sun, B.-C. Shih, P. Dev, S. B. Zhang, and P. Zhang, Dynamic Jahn-Teller Effect in the NV$^-$ Center in Diamond, Phys. Rev. Lett. **107**, 146403 (2011).

[46] U. Levy and Y. Silberberg, Weakly diverging to tightly focused Gaussian beams: A single set of analytic expressions, J. Opt. Soc. Am. A **33**, 1999 (2016).